

Spectroscopic signatures of magnetospheric accretion in Herbig Ae/Be stars.

I. The case of HD 101412.*

M. Schöller¹, M. A. Pogodin², J. A. Cahuaqui³, N. A. Drake^{4,5}, S. Hubrig⁶, M. G. Petr-Gotzens¹, I. S. Savanov⁷,
B. Wolff¹, J. F. González⁸, S. Mysore¹, I. Ilyin⁶, S. P. Järvinen⁶, and B. Stelzer⁹

¹ European Southern Observatory, Karl-Schwarzschild-Str. 2, 85748 Garching, Germany
e-mail: mschoell@eso.org

² Central Astronomical Observatory at Pulkovo, Pulkovskoye chaussee 65, 196140 Saint Petersburg, Russia

³ I. Physikalisches Institut, Universität zu Köln, Zùlpicher Str. 77, 50937 Köln, Germany

⁴ Saint Petersburg State University, Universitetskiy pr. 28, 198504 Saint Petersburg, Russia

⁵ Observatório Nacional/MCTI, Rua General José Cristino 77, CEP 20921-400, Rio de Janeiro, RJ, Brazil

⁶ Leibniz-Institut für Astrophysik Potsdam (AIP), An der Sternwarte 16, 14482 Potsdam, Germany

⁷ Institute of Astronomy, Russian Academy of Sciences, Pyatnitskaya 48, 119017 Moscow, Russia

⁸ Instituto de Ciencias Astronómicas, de la Tierra y del Espacio (ICATE), 5400 San Juan, Argentina

⁹ INAF - Osservatorio Astronomico di Palermo, Piazza del Parlamento 1, 90134 Palermo, Italy

Received ????? ???, ???; accepted ????? ??, ???

ABSTRACT

Context. Models of magnetically-driven accretion and outflows reproduce many observational properties of T Tauri stars. This concept is not well established for the more massive Herbig Ae/Be stars.

Aims. We intend to examine the magnetospheric accretion in Herbig Ae/Be stars and search for rotational modulation using spectroscopic signatures, in this first paper concentrating on the well-studied Herbig Ae star HD 101412.

Methods. We used near-infrared spectroscopic observations of the magnetic Herbig Ae star HD 101412 to test the magnetospheric character of its accretion disk/star interaction. We reduced and analyzed 30 spectra of HD 101412, acquired with the CRIRES and X-shooter spectrographs installed at the VLT (ESO, Chile). The spectroscopic analysis was based on the He I $\lambda 10,830$ and Pa γ lines, formed in the accretion region.

Results. We found that the temporal behavior of these diagnostic lines in the near-infrared spectra of HD 101412 can be explained by rotational modulation of line profiles generated by accreting gas with a period $P = 20^d53 \pm 1^d68$. The discovery of this period, about half of the magnetic rotation period $P_m = 42^d076$ previously determined from measurements of the mean longitudinal magnetic field, indicates that the accreted matter falls onto the star in regions close to the magnetic poles intersecting the line-of-sight two times during the rotation cycle. We intend to apply this method to a larger sample of Herbig Ae/Be stars.

Key words. Stars: pre-main sequence – Accretion – Stars: magnetic field – Stars: individual: HD 101412

1. Introduction

Herbig Ae/Be stars (HAeBes) are pre-main-sequence (PMS) objects with pronounced emission line features and an infrared (IR) excess indicative of dust in their circumstellar (CS) disks (Herbig 1960; Finkenzeller & Mundt 1984; Thé et al. 1994). It is now recognized that these stars are intermediate-mass analogues of T Tauri stars, but with convectively stable interiors that do not support dynamo action as found in the fully convective T Tauri stars (Gullbring et al. 1998). For this reason, unlike for the T Tauri stars, strong magnetic fields of the order of 1 kG are usually not expected in HAeBes. On the other hand, in recent years a number of magnetic studies revealed that some Herbig Ae/Be stars have globally organized magnetic fields of the order of 100 G (Hubrig et al. 2004; Wade et al. 2005; Alecian et al. 2008; Hubrig et al. 2009; Alecian et al. 2013; Hubrig et al. 2013; Hubrig et al. 2015). From detailed magnetohydrodynamical

models, it is expected that magnetic fields in low-mass PMS objects funnel material from the disk towards the star and launch a collimated bipolar outflow (Shu et al. 2000). The star/CS interaction in classical T Tauri stars is well described by the magnetospheric accretion (MA) model (Bouvier et al. 2007), where the field truncates the disk at a distance of between five and ten stellar radii. However, it is still unclear how well this model can be applied to HAeBes, whose magnetic fields are roughly one order of magnitude weaker.

Recently, Cauley & Johns-Krull (2014) presented results of an analysis of the He I $\lambda 10,830$ profile morphologies for a significant sample of more than 50 HAeBes in a wide range of spectral types. They concluded that objects of early B types show no sign of the MA process. The matter infall from their disks onto the star takes place near the equatorial plane. On the other hand, the He I $\lambda 10,830$ profile shape in the spectra of objects of late B and A types indicates that they are surrounded by magnetospheres, but with radii much smaller than in the case of T Tauri stars. This result is not surprising, taking into account the lower values of their magnetic fields (Hubrig et al. 2015). Clearly, important di-

* Based on observations made with ESO Telescopes at the La Silla Paranal Observatory under programme IDs 087.C-0124(A), 088.C-0218(A,B,C,E), 090.C-0331(A), and 092.C-0126(A).

agnostics of the star/CS interaction region of individual objects are accessible by examining the temporal behavior of near-IR spectral lines of these objects.

In our studies, we aim to investigate the accretion process and test the applicability of the MA model to selected Herbig Ae/Be stars with previously detected magnetic fields, concentrating in this first paper on the well-studied Herbig Ae star HD 101412. Our method is based on monitoring the variability detected in the red part of line profiles originating in (or close to) the region of the star/CS interaction. If the orientation of the disk deviates from an edge-on orientation, then the detected variability can be considered as a signature of the accretion flows intersecting the line-of-sight at intermediate and high latitudes. This can take place only for MA accretion, when the accreted material is carried out from the equatorial plane along closed magnetic field lines inside the magnetosphere to higher latitudes.

We also intend to search for rotational modulation in spectral line profiles. If the star has a significant magnetosphere and the magnetic axis is not aligned with the rotation axis, the accreted flow will be governed by the magnetic field inside the magnetosphere and the accretion shock on the stellar surface near the magnetic pole will be observed as an azimuthal inhomogeneity. Such an inhomogeneity rotates together with the star and modulates the line shape with a period equal to the rotation period of the star.

More specifically, we investigate the variability observed in two near-IR lines, He I $\lambda 10,830$ and Pa γ (at $10,938 \text{ \AA}$), in the spectrum of the strongly magnetic Herbig Ae star HD 101412. The important role of these lines in probing the structure of the accretion region of PMS objects has already been discussed by Edwards et al. (2006).

Hubrig et al. (2010) studied spectra of HD 101412 obtained with UVES and HARPS and identified resolved magnetically split lines indicative of a variable magnetic field modulus, changing from 2.5 to 3.5 kG. Such a strong field is typical for T Tauri stars, but is rarely measured in HAeBe stars. A study of the magnetic variability of HD 101412 found a cyclical variation of the mean longitudinal magnetic field $\langle B_z \rangle$ with an amplitude of $A_{\langle B_z \rangle} = 465 \pm 27 \text{ G}$ around a mean value of $\langle B_z \rangle = 9 \pm 18 \text{ G}$ (Hubrig et al. 2011). HD 101412 rotates very slowly, with a projected rotation velocity of $v \sin i \approx 3 \text{ km s}^{-1}$ (Cowley et al. 2010). Using the stellar fundamental parameters and the detected magnetic rotation period of $P_m = 42^d 076 \pm 0^d 017$, the inclination angle of the rotation axis relative to the line-of-sight was estimated as $i = 80 \pm 7^\circ$, and the angle between the magnetic and the rotation axis was determined as $\beta = 84 \pm 13^\circ$ (Hubrig et al. 2011). This means that the magnetic axis lies close to the plane of the equatorial disk, and that the regions close to the magnetic poles, where the accreted matter falls onto the star, intersect the line-of-sight two times during one rotation period.

2. Observations and data reduction

The spectra of HD 101412 were acquired with CRIRES (Cryogenic high-resolution InfraRed Echelle Spectrograph) in short wavelength ranges around the He I $\lambda 10,830$ and Pa γ lines with a spectral resolution of $R \sim 100,000$, and using X-shooter ($R \sim 11,000$) to obtain spectral data simultaneously over the entire spectral range from the near-UV to the near-IR in three different arms. Both instruments are operated by the European Southern Observatory (ESO) on the Very Large Telescope (VLT) on Cerro Paranal, Chile. In total, 30 spectra were obtained from 2011 to 2014. The full list of observations is presented in

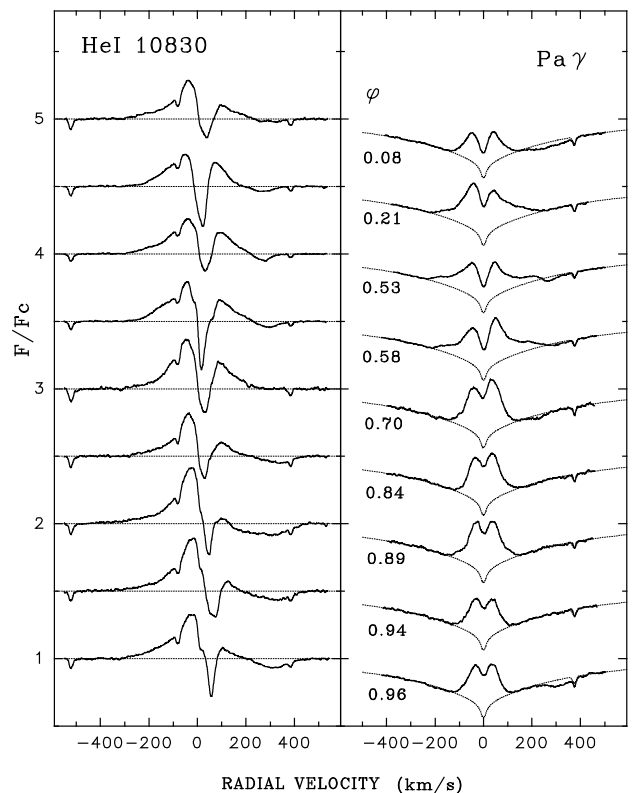


Fig. 1. Line profiles of the He I $\lambda 10,830$ and Pa γ lines in HD 101412 CRIRES spectra. Rotation phases of the observations assuming the magnetic rotation period $P_m = 42^d 076$ are presented close to the Pa γ lines. From top to bottom, these phases correspond to observations obtained at MJD 55662.082, 55667.174, 55681.023, 55683.058, 56361.178, 56367.283, 55654.085, 55656.062, and 56372.185 (see Table B.1). The epoch MJD 52797.4 corresponds to phase $\varphi = 0$, as presented in Fig. 4 of Hubrig et al. (2011). Synthetic Pa γ profiles assuming the atmospheric parameters $T_{\text{eff}} = 8300 \text{ K}$ and $\log g = 3.8$ are indicated by the dotted lines.

Table B.1, where Col. 1 gives the modified Julian date (MJD) at the middle time of observation, Col. 2 the instrument used, Col. 3 the signal-to-noise ratio (S/N) reached in the continuum between the He I $\lambda 10,830$ and Pa γ lines, and Col. 4 the phase corresponding to the ephemerides presented by Hubrig et al. (2011). A S/N of 100–500 was achieved for all spectra observed. Both CRIRES and X-shooter spectra were reduced using the respective ESO pipeline. The normalization of the spectra near Pa γ was carried out using a photospheric synthetic spectrum calculated with the code SYNTH3 (Kochukhov 2007). We assumed the atmospheric parameters $T_{\text{eff}} = 8300 \text{ K}$ and $\log g = 3.8$ (Cowley et al. 2010) and made use of the VALD atomic line database (Kupka et al. 1999).

3. Spectroscopic signatures of magnetospheric accretion

The profiles of the He I $\lambda 10,830$ and Pa γ lines observed in the CRIRES spectra of HD 101412 are presented in Fig. 1; a presentation of the X-shooter data can be found in Fig. A.1. The He I line appears as an emission profile with two separate redshifted absorptions. The first of them, narrow and deep, shows a small velocity shift towards the red, typically at locations between 20

and 70 km s^{-1} . The second absorption in the red is much wider. It is rather flat and demonstrates a large velocity shift, starting as low as 100 km s^{-1} and ending as high as 500 km s^{-1} . Similar wide redshifted absorptions are observed also in the Pay profiles on a few observing epochs. All components in both line profiles are variable in intensity, shape and velocity. Only the central absorption component in the Pay profile shows no velocity shift.

The behavior of the near-IR lines in the spectrum of HD 101412 is closely related to the edge-on orientation of the accretion disk and the matter flows falling onto the star from the inner edge of the disk. Applying the magnetic field model of Hubrig et al. (2011), it follows that the accretion onto the star occurs as a flow with two components related to the two magnetic polar regions. The broad redshifted absorption is formed in the infalling flows screening the stellar disk near these magnetic polar regions. The central absorption originates from the inner part of the disk. The high-temperature region of the He I formation is geometrically thinner than in the case of Pay. It covers the volume where the accretion is just beginning, whereas the central Pay absorption is generated in a spatially more extended region, where the accreted flows are not yet significant. An illustration of the principal components in a typical MA model is given, for example, in Camenzind (1990).

It can be seen in Fig. 1 that the width of the emission profiles of the He I line are systematically larger than those of the Pay line. This phenomenon can be a result of additional emission that is present in emission wings of lines, connected with the stellar wind and the accretion flows at higher latitudes, which do not screen the stellar disk due to the edge-on orientation of the object. According to the MA model, for a wind being driven along open magnetic field lines, the field enforces corotation out to approximately the Alfvén radius R_A (Cauley & Johns-Krull 2014). Inside R_A , the outflowing gas is accelerated by the magnetic centrifuge and becomes less dense due to the open field configuration and mass conservation. A high-velocity wind of low density at a distance near R_A is much better registered in the resonance He I line than in the subordinate Pay line, which is very sensitive to the gas density. Emission in Pay can appear only in gas with a density sufficiently higher than that in the remote wind.

Assuming the presence of two streams passing the line-of-sight and screening the star two times during one rotation period, we expect two times an increase of the broad redshifted absorption in the line profiles and a decrease of the intensity of the emission components. This takes place because screening the star by a stream leads to absorption of stellar radiation by the infalling matter. The brightness of the stream itself in the considered lines is lower than that of the stellar disk. Thus, the absorbing effect from a stream passing is sufficiently stronger than the effect from its additional emission. As a result, the broad absorption components have to appear at large positive velocities, where there is no emission from the disk. Further, a decrease in the intensity of the emission profile is observed at velocities where the disk emission overlaps with the radiation of star and stream.

To investigate the temporal behavior of the spectral lines, we used specific line parameters characterizing the change in the broad red absorption component and the intensity variability of the line emission. v_{r1} and v_{r2} are the velocities of the blue and the red edges of the broad redshifted absorption of the He I line at the continuum level. In the case of Pay, this absorption component is not present in all observations. For this line, we used the parameter v_{red} , which is the velocity of the red edge of the emission profile. We assume that this parameter is an analog

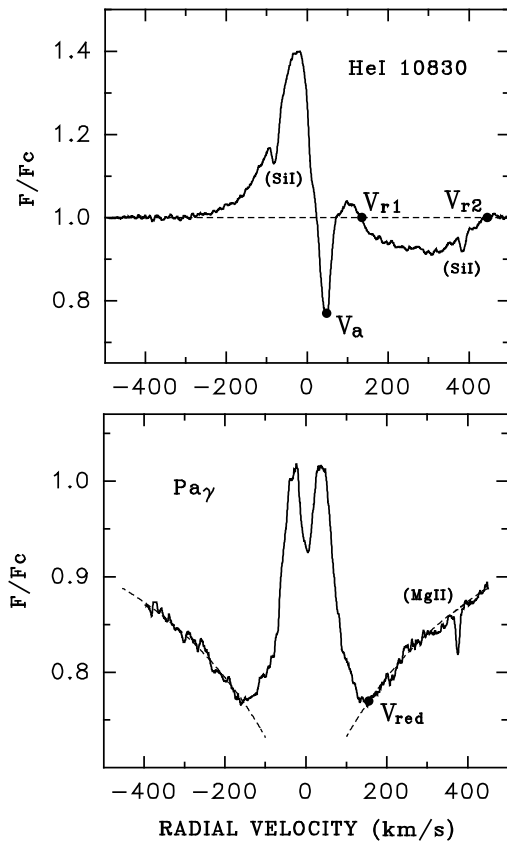


Fig. 2. Spectral parameters of the He I $\lambda 10,830$ and Pay line profiles used in the quantitative analysis.

of v_{r1} when the broad red absorption is not detectable in our spectra and manifests itself as a depression of the red emission wing. The parameter EW is the equivalent width of an emission profile above the atmospheric background (determined as $F_{line}/F_{cont} - 1$). Additionally, we used the parameter v_a , which is the velocity of the deep central absorption of the He I line, which is formed at the high-temperature inner boundary of the disk and is an indicator of the origin of the accretion process. The exact locations of these parameters are illustrated in Fig. 2. The measured values of all line parameters, together with the measurement accuracies obtained at different dates, are presented in Cols. 5–10 of Table B.1. The determination of the EW errors follows Smith et al. (1995). The errors in velocity are deduced from a wavelength calibration term and twice the error of the gradient of the line profile. With CRIRES, we obtain errors of 20 m\AA for the EW and between 1 and 30 km s^{-1} for the velocities. For X-shooter, errors are typically a factor of 2 to 3 larger.

The assumption of the presence of rotating streams as a cause for the observed variability of the line parameters implies the existence of correlations between their variations. One can expect a direct correlation between the EWs of the He I and Pay lines, and between the EWs of both lines and the parameters v_{r1} (He I) and v_{red} (Pay). An inverse correlation is expected between all these parameters and v_{r2} (He I). Before studying such correlations, we must eliminate long-term variabilities that are not connected with the rotation of the stream. The temporal behavior of the EW for both IR lines is illustrated in Fig. 3. A systematic difference is detected between values of EW(He I) obtained in the four observing periods MJD 55650–55690, MJD 55940–56010, MJD 56360–56370, and MJD 56630–56720. In the case of the EW(Pay), a similar difference was observed only for

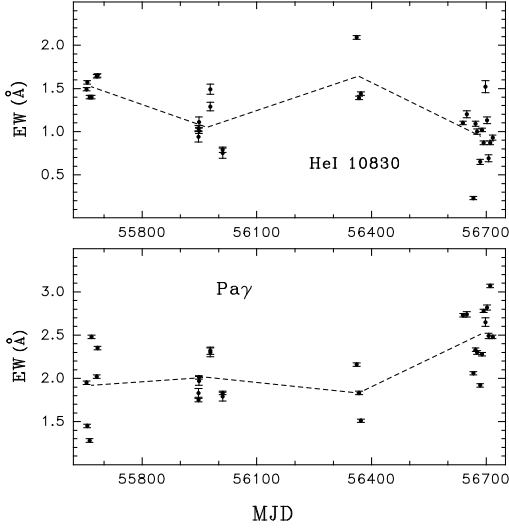


Fig. 3. Temporal behavior of the EW of the He I $\lambda 10,830$ and Pa γ lines. Linear trends between the time intervals of the observations are indicated by the dashed lines, connecting the mean values observed in each epoch. Error bars are indicated for all values.

the values observed in the fourth observing period. No long-term variations were detected in the temporal behavior of the other line parameters. To eliminate the effect of long-term variability of the EWs, which was assumed to be a linear trend between the four observing periods, all values corresponding to the first three periods were divided by the ratio of the mean values of the EWs calculated separately for the first three periods and that for the fourth period. As a result, four relevant correlations have been revealed and the corresponding correlation coefficient r determined:

$$v_{r1}(\text{He I}) \text{ vs. } EW(\text{He I}) : r = +0.65 \pm 0.10, \quad (1)$$

$$v_{r1}(\text{He I}) \text{ vs. } v_{r2}(\text{He I}) : r = -0.73 \pm 0.08, \quad (2)$$

$$v_{r1}(\text{He I}) \text{ vs. } v_{\text{red}}(\text{Pa}\gamma) : r = +0.64 \pm 0.11, \quad (3)$$

$$v_{\text{red}}(\text{Pa}\gamma) \text{ vs. } EW(\text{Pa}\gamma) : r = +0.70 \pm 0.09. \quad (4)$$

with the error of r determined by $(1-r^2)/\sqrt{N}$ and N the number of the measured values (see equation 26.24 in Kendall & Stuart 1961).

The existence of such correlations indicates the presence of accreted matter between the star and the observer. The discovery of such correlations would be enough to confirm the MA character of the accretion in an object with an intermediate disk orientation. But in the case of an edge-on oriented object like HD 101412, where the accretion process takes place practically in the equatorial plane, such correlations can occur not only as a result of the presence of rotating streams, but also due to a change of parameters of the accretion process in absence of a magnetosphere. Only the detection of a rotational modulation of the line profiles can be considered a convincing signature of the magnetospheric accretion.

4. Periodicity search using the spectroscopic signatures

As outlined above, it is important to search for signatures of rotational modulation in the different line profile parameters to confirm the existence of a cyclic variability with a period near half

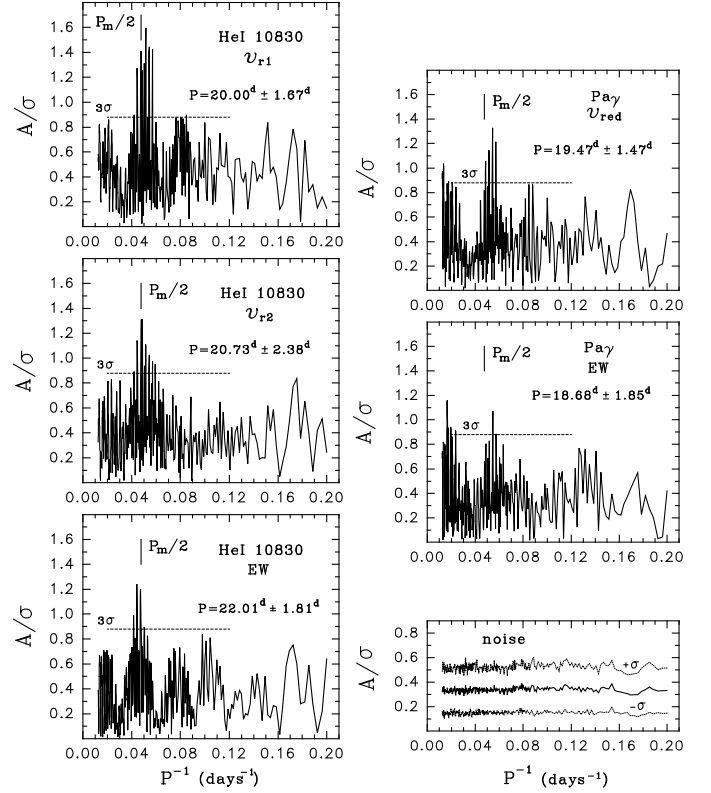


Fig. 4. Different line parameters' A/σ periodograms as defined in Sect. 3. Significance levels of 3σ are indicated by the dashed lines. Short vertical lines indicate the value corresponding to half of the magnetic rotation period ($P_m/2 = 21^d038$). The detected period values and their errors are given in each plot.

the magnetic rotation period of HD 101412 detected by Hubrig et al. (2011), that is with a period of about 21 d.

From a simple geometric consideration, variability related to rotational modulation is expected to show a sine character if $\beta + i < 90^\circ$, when only one magnetic pole is visible to the observer during the rotation period. For other cases, when both poles are observed over the rotation cycle, the character of the modulation can be more complex and it is possible to describe it by a function with several sinusoidal harmonics. We note that we do not intend to investigate this character in detail since our data set is not large enough for such an analysis. We try only to confirm a periodicity of the parameter variations and to estimate the value of the period. For this reason, we used the simplest method of harmonic analysis with only one harmonic. As we show below, this method allows us to achieve more precise results than other methods not connected with a harmonic analysis, for example, the method of Laefer & Kinman (1965).

Our search for periodicity is based on fitting phase dependencies for each value of the trial period P with a sine for a range of 5 to 80 days, in steps of 0.1 days. The parameters of the sine, amplitude, constant coefficient, and initial phase, were determined using the ordinary least-square method for each value of P . We applied this method to the diagnostic line parameters introduced in the previous section. The periodogram for v_a turned out not to be informative. This parameter traces the region of the inner disk where the accretion starts, which might be viewed differently for the two magnetic poles due to the disk not being fully edge-on and the magnetic field not exactly perpendicular to the rotation axis. The periodograms constructed for

the other five parameters are shown in Fig. 4. A/σ is the ratio between the amplitude of the sinusoid and the standard deviation of the residuals of the sine function fit for a given P . To determine the window function and to estimate the significance level of the separate peaks in the periodograms, we also calculate the noise periodogram, following closely the methods employed by Zechmeister & Kürster (2009) and Alvarado-Gómez et al. (2015). It was constructed by substituting the line parameter values in the temporal sequence by a set of random numbers and the calculation of a periodogram with the same series of dates. More than 200 reiterations of this procedure allowed us to generate a mean noise periodogram and the standard deviation of an individual periodogram relative to the mean (Fig. 4, plot on bottom right).

A peak near half the magnetic rotation period $P_m/2$ is seen in all periodograms at a significance level higher than 3σ . Each peak is rather wide and consists of several narrow local peaks. Such a structure is the result of a) the rather low number of observations and b) the non-uniform distribution of all values over the observing dates, with the temporal sequence divided into four separate groups (see Fig. 3). The positions of the local peaks inside each wide peak allow us to estimate the mean value P and the standard deviation for the given peak, which are indicated in Fig. 4.

To test our method of period determination, we carried out independent period estimations using the standard Lomb normalized periodogram (LNP) based on an IDL (Interactive Data Language) routine following Press et al. (1992). This analysis led to practically identical periodograms including positions and relative amplitudes of all local peaks inside the main wide peaks.

The most significant periods are the periods determined using the parameters of the He I line (Fig. 4, left panels). In the periodograms calculated for Pa γ (Fig. 4, upper two panels on the right), a period near $P_m/2$ is not so obvious, some other periods at significant levels are also seen at $P \sim 50^d$ and $P \sim 8^d$. Since the window function is rather smooth for our temporal sequence (Fig. 4, bottom right), these additional periods cannot be a result of the specific data distribution over time. Sometimes such period-artifacts can appear accidentally, as a result of poor statistics. We tested whether several periods present in the periodograms constructed for the Pa γ parameters are independent from each other. The periodogram calculation was repeated, but a sine corresponding to $P \sim 21^d$ was first subtracted from the temporal sequence. It turned out that the periods at $P \sim 50^d$ and $P \sim 8^d$ disappeared too. This means that the periodograms contain artifacts related to poor statistics. In this case, the repetition of the period appearance in all periodograms can be a criterion of its validity. The only real period is that near $P_m/2$.

We also obtained the mean periodogram, averaging the periodograms from all five parameters. As a result, we found the period of variation of the spectroscopic data $P = 20^d53 \pm 1^d68$, which is in good agreement with half the magnetic rotation period $P_m/2 = 21^d038$. For comparison, a similar estimate made with the Laefler-Kinman method resulted in $P = 20^d49 \pm 2^d48$.

Fig. 5 illustrates the phase dependencies of the different line parameters constructed for $P_m = 42^d076$ and the initial phase $\varphi = 0$ at MJD 52797.4 taken from Hubrig et al. (2011). Phases where $\langle B_z \rangle$ reaches its maximum and minimum values are marked in the figure. One can see that the value of the $v_{r2}(\text{He I})$ parameter reaches its maximum just at the phases where $\langle B_z \rangle$ is at its minimum or maximum. $v_a(\text{He I})$ shows a maximum only during the phase when $\langle B_z \rangle$ has a minimum, and with a smaller amplitude than $v_{r2}(\text{He I})$. As the MA model predicts, the values of such parameters as $v_{r1}(\text{He I})$, $v_{\text{red}}(\text{Pa}\gamma)$, and EW (for

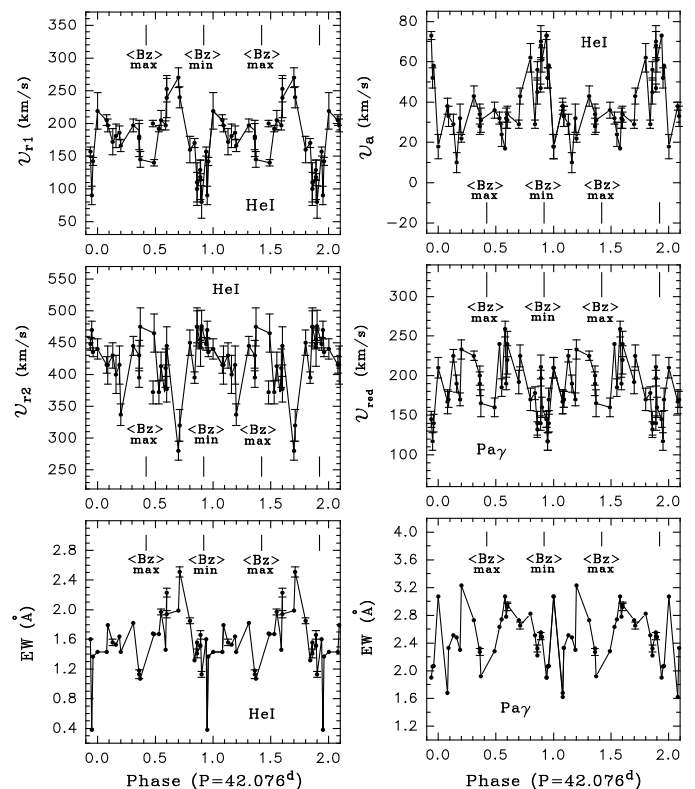


Fig. 5. Phase dependencies of different line parameters over the magnetic rotation period $P_m = 42^d076$. The initial phase $\varphi = 0$ corresponds to MJD 52797.4. Error bars are given for each value.

both lines) become minimal at phases where $\langle B_z \rangle$ reaches its minimum or maximum values.

We conclude that the phase dependencies of all chosen line parameters are in good agreement with an MA model and with the magnetic field topology and orientation suggested by Hubrig et al. (2011). The phases when $\langle B_z \rangle$ takes its maximum and minimum values correspond to the times when the magnetic poles are close to the line-of-sight. At these phases, the matter flows move exactly away from the observer, screening the star. This results in a decrease of the EW values of the spectral lines and a growth of the broad redshifted absorptions followed by an increase of $v_{r2}(\text{He I})$ and $v_a(\text{He I})$ and a decrease of $v_{r1}(\text{He I})$ and $v_{\text{red}}(\text{Pa}\gamma)$. Interestingly, during our study of the rotational modulation, we noticed that the value scatter in a number of phase dependencies is much larger than the observational errors indicated in Table B.1, especially for the EW. This means that the line parameters exhibit additional variability not directly connected to the rotational modulation. It is likely to be the result of a change in the accretion regime on different timescales.

5. Conclusions

According to Romanova et al. (2003, 2004) and Romanova & Owocki (2015), magnetospheric accretion is a complex process, and the interaction between the inner disk matter and the stellar magnetosphere depends on a number of factors, such as the star's rotation period, the structure of the stellar magnetic field, the size of the magnetosphere, the diffusivity at the disk-magnetosphere boundary, properties of the accretion disk, and other elements. Numerical global 3D MHD simulations of accretion onto stars with different tilt angles of the dipole field have been performed by Romanova et al. (2003, 2004). The authors

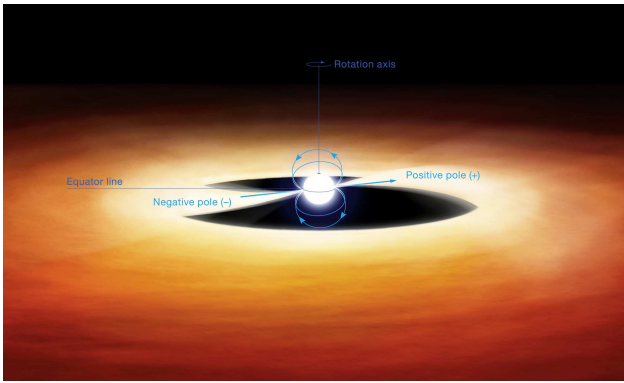


Fig. 6. Artist's impression of the magnetospheric accretion in HD 101412, looking at the magnetic equator (corresponding to rotation phase 0.25). The viewing and obliquity angles follow the model determined by Hubrig et al. (2011). The exact size and shape of both the disk and the accretion streams are for illustration only, since we lack constraints on these parameters.

showed that for dipole inclination angles larger than 60° , matter accretes in two streams that follow paths to the closest magnetic pole. The streams have a shape different from those at small inclination angles and come to the star near the equatorial plane. The accretion rate is smaller for aligned dipoles than for tilted dipoles. Further, the variability of different spectral lines is expected to depend on the density, temperature, and velocity distributions along the line of sight to the star. Since the He I $\lambda 10,830$ line probes inflow (accretion) and outflow (winds) in the star-disk interaction region of accreting T Tauri and Herbig Ae stars (Edwards et al. 2006; Fischer et al. 2008), it can be successfully used to study the influence of magnetic field topologies on the star-disk interaction. Revealing the relations between the mass accretion rate and the magnetic field geometry is very promising since they can constrain the predictions of theoretical studies of magnetospheric accretion and wind launching models.

The results of our spectroscopic study of the strongly magnetic Herbig Ae star HD 101412 show that the temporal behavior of its near-IR lines He I $\lambda 10,830$ and Pa γ , originating from the region of the star/CS interaction, can be successfully explained in the framework of a magnetospheric accretion model with the geometry of the magnetic field suggested by Hubrig et al. (2011). In Fig. 6, we present an artist's impression of the topology of the MA in HD 101412, as seen by an observer when looking onto the magnetic equator. The average period $P = 20^d53 \pm 1^d68$ has been detected from the modulation of a number of line profile parameters, and is in good agreement with half the magnetic rotation period $P_m/2 = 21^d038$. It is of great importance to apply the same procedure to other Herbig Ae/Be stars to determine their rotation periods and to probe the structure of their accretion regions (see e.g. Table 2 of Hubrig et al. 2015).

Acknowledgements. We would like to thank the ESO education and Public Outreach Department and especially Mafalda Martins for providing Fig. 6. This work was supported by the Basic Research Program of the Presidium of the Russian Academy of Sciences P-41 and the Program of the Department of Physical Sciences of the Russian Academy of Sciences P-17. N.A.D. acknowledges the support of FAPERJ, Rio de Janeiro, Brazil, for Visiting Researcher grant E-26/200.128/2015 and the St. Petersburg State University for research grant 6.38.18.2014.

References

Alecian, E., Catala, C., Wade, G. A., et al. 2008, MNRAS, 385, 391

- Alecian, E., Wade, G. A., Catala, C., et al. 2013, MNRAS, 429, 1001
 Alvarado-Gómez, J. D., Hussain, G. A. J., Grunhut, J., et al. 2015, A&A, 582, A38
 Bouvier, J., Alencar, S. H. P., Harries, T. J., Johns-Krull, C. M., & Romanova, M. M. 2007, in Protostars and Planets V, ed. B. Reipurth, D. Jewitt, & K. Kaul (Tucson: Univ. Arizona Press), 479
 Camenzind, M. 1990, Rev. in Modern Astronomy, 3, 234
 Cauley, P. W., & Johns-Krull, C. M. 2014, ApJ, 797, 112
 Cowley, C. R., Hubrig, S., González, J. F., & Savanov, I. 2013, A&A, 523, 65
 Edwards, S., Fischer, W., Hillenbrand, L., & Kwan, J. 2006, ApJ, 646, 319
 Finkenzeller, U., & Mundt, R. 1984, A&ASS, 55, 109
 Fischer, W., Kwan, J., Edwards, S., & Hillenbrand, L. 2008, ApJ, 687, 1117
 Gullbring, E., Hartmann, L., Briceño, C., & Calvet, N. 1998, ApJ, 492, 323
 Herbig, G. H. 1960, ApJS, 4, 33
 Hubrig, S., Schöller, M., & Yudin, R. V. 2004, A&A, 428, L1
 Hubrig, S., Stelzer, B., Schöller, M., et al. 2009, A&A, 502, 283
 Hubrig, S., Schöller, M., Savanov, I., et al. 2010, Astr. Nachr., 331, 361
 Hubrig, S., Mikulášek, Z., González, J. F., et al. 2011, A&A, 525, L4
 Hubrig, S., Schöller, M., Ilyin, I., & Lo Curto, G. 2013, AN, 334, 1093
 Hubrig, S., Carroll, T. A., Schöller, M., & Ilyin, I. 2015, MNRAS, 449, L118
 Kendall, M. G., & Stuart, A. 1961, The Advanced Theory Of Statistics, p. 292
 Kochukhov, O. 2007, in Physics of Magnetic Stars, ed. I. I. Romanyuk, & D. O. Kudryavtsev, 109
 Kupka, F., Piskunov, N. E., Ryabchikova, T. A., Stempels, H. C., & Weiss, W. W. 1999, A&A, 138, 119
 Laeffer, J., & Kinman, T. D. 1965, ApJS, 11, 216
 Press, W. H., Teukolsky, S. A., Vetterling, W. T., & Flannery, B. P. 1992, Numerical Recipes. The Art of Scientific Computing (Second Edition). Section 13.8 (C).
 Romanova, M. M., Ustyugova, G. V., Koldoba, A. V., Wick, J. V., & Lovelace, R. V. E. 2003, ApJ, 595, 1009
 Romanova, M. M., Ustyugova, G. V., Koldoba, A. V., & Lovelace, R. V. E. 2004, ApJ, 610, 920
 Romanova, M. M., & Owocki, S. P. 2015, Space Sci. Rev., 191, 339
 Shu, F. H., Najita, J. R., Shang, H., & Li, Z.-Y. 2000, in Protostars and Planets IV, ed. V. Mannings, A. P. Boss, & S. S. Russell (Tucson: Univ. Arizona Press), 789
 Smith, V. V., Cunha, K., & Lambert, D. L. 1995, AJ, 110, 2827
 Thé, P. S., de Winter, D., & Pérez, M. R. 1994, A&AS, 104, 315
 Wade, G. A., Drouin, D., Bagnulo, S., et al. 2005, A&A, 442, L11
 Zechmeister, M., & Kürster, M. 2009, A&A, 496, 577

Appendix A: The X-shooter data set

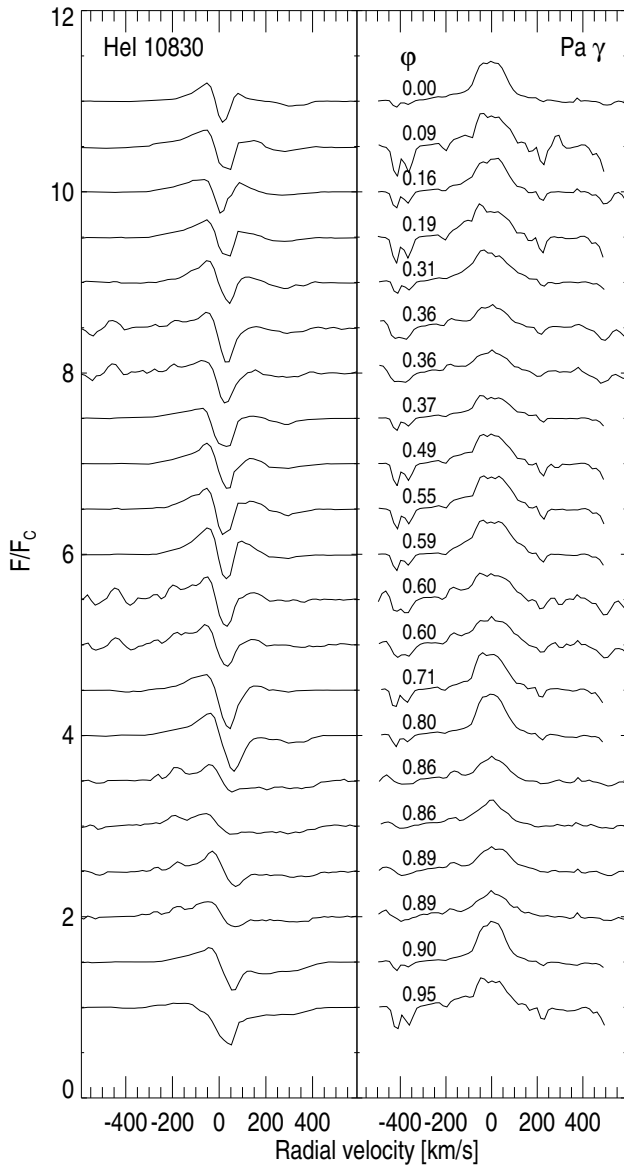


Fig. A.1. Line profiles of the He I $\lambda 10,830$ and Pa γ lines in HD 101412 X-shooter spectra. The rotation phases of the observations assuming the magnetic rotation period $P_m = 42^d.076$ are presented close to the Pa γ lines.

Appendix B: Data sets and determined spectral parameters

Table B.1. List of the HD 101412 spectra and parameters of the line profiles. φ is the phase of the magnetic rotation period following Hubrig et al. (2011). EW is the equivalent width (determined as $F_{\text{line}}/F_{\text{cont}} - 1$), v_{r1} and v_{r2} are the velocities of the blue and red edges of the broad absorption component of the He I $\lambda 10,830$ line profile component. v_{red} is the velocity of the red edge of the Pay emission and v_a is the velocity of the central He I $\lambda 10,830$ absorption. The errors of the measurements are given in brackets.

MJD	Instrument	S/N	φ	He I $\lambda 10,830$				Pay	
				EW [Å]	v_{r1} [km s ⁻¹]	v_{r2} [km s ⁻¹]	v_a [km s ⁻¹]	EW [Å]	v_{red} [km s ⁻¹]
55654.085	CRIFES	280	0.89	1.49 (0.02)	136 (5)	465 (6)	47 (2)	1.95 (0.02)	140 (9)
55656.062	CRIFES	270	0.94	1.57 (0.02)	180 (7)	465 (10)	73 (1)	1.45 (0.02)	145 (10)
55662.082	CRIFES	350	0.08	1.40 (0.02)	236 (8)	430 (13)	38 (2)	1.28 (0.02)	167 (15)
55667.174	CRIFES	410	0.21	1.40 (0.02)	191 (9)	350 (17)	22 (2)	2.48 (0.02)	233 (12)
55681.023	CRIFES	480	0.53	1.64 (0.02)	220 (5)	385 (18)	32 (3)	2.01 (0.02)	240 (3)
55683.058	CRIFES	420	0.58	1.65 (0.02)	228 (5)	385 (18)	17 (1)	2.35 (0.02)	259 (10)
55947.273	X-shooter	180	0.86	1.04 (0.03)	120 (30)	479 (30)	56 (4)	1.75 (0.02)	132 (10)
55947.276	X-shooter	120	0.86	0.94 (0.06)	76 (25)	484 (25)	45 (6)	1.83 (0.05)	140 (15)
55948.351	X-shooter	160	0.89	1.01 (0.03)	105 (15)	460 (15)	68 (7)	2.01 (0.02)	197 (10)
55948.354	X-shooter	120	0.89	1.11 (0.06)	93 (30)	450 (30)	70 (8)	1.97 (0.05)	211 (15)
55978.200	X-shooter	130	0.60	1.49 (0.06)	205 (20)	380 (20)	31 (4)	2.30 (0.05)	220 (18)
55978.202	X-shooter	100	0.60	1.29 (0.05)	195 (30)	450 (30)	34 (4)	2.32 (0.04)	240 (16)
56010.262	X-shooter	160	0.36	0.75 (0.06)	170 (20)	400 (24)	34 (5)	1.79 (0.05)	200 (12)
56010.265	X-shooter	110	0.36	0.79 (0.03)	178 (28)	380 (15)	28 (4)	1.83 (0.02)	190 (15)
56361.178	CRIFES	190	0.70	2.09 (0.02)	275 (15)	280 (15)	29 (2)	2.16 (0.02)	192 (15)
56367.283	CRIFES	280	0.84	1.39 (0.02)	229 (7)	430 (9)	29 (2)	1.83 (0.02)	178 (8)
56372.185	CRIFES	260	0.96	1.44 (0.02)	190 (6)	475 (7)	58 (1)	1.51 (0.02)	140 (11)
56639.267	X-shooter	250	0.31	1.10 (0.02)	197 (10)	445 (15)	43 (5)	2.73 (0.02)	225 (6)
56649.336	X-shooter	110	0.55	1.20 (0.04)	205 (15)	413 (22)	24 (6)	2.74 (0.03)	185 (11)
56666.302	X-shooter	240	0.95	0.23 (0.02)	90 (14)	470 (14)	52 (5)	2.06 (0.02)	116 (4)
56672.163	X-shooter	230	0.09	1.09 (0.03)	197 (10)	415 (30)	33 (5)	2.33 (0.02)	170 (10)
56676.246	X-shooter	160	0.19	1.00 (0.03)	186 (10)	415 (30)	32 (7)	2.30 (0.02)	170 (8)
56684.194	X-shooter	220	0.37	0.65 (0.03)	145 (12)	475 (30)	31 (6)	1.92 (0.02)	165 (17)
56689.183	X-shooter	320	0.49	1.02 (0.02)	140 (6)	465 (30)	36 (4)	2.28 (0.02)	160 (12)
56693.316	X-shooter	250	0.59	0.87 (0.02)	197 (7)	410 (30)	32 (5)	2.78 (0.02)	190 (8)
56698.103	X-shooter	150	0.71	1.53 (0.07)	240 (16)	320 (25)	43 (4)	2.65 (0.05)	225 (14)
56702.087	X-shooter	150	0.80	1.13 (0.04)	160 (20)	450 (20)	62 (7)	2.82 (0.03)	170 (14)
56706.088	X-shooter	160	0.90	0.69 (0.04)	80 (25)	476 (25)	61 (6)	2.49 (0.03)	160 (13)
56710.367	X-shooter	330	0.00	0.87 (0.02)	219 (28)	440 (16)	18 (6)	3.07 (0.02)	210 (13)
56717.047	X-shooter	310	0.16	0.93 (0.03)	181 (18)	400 (30)	10 (5)	2.48 (0.02)	190 (11)